

# Journal of Biomedical Optics

BiomedicalOptics.SPIEDigitalLibrary.org

## **Comparison between optical-resolution photoacoustic microscopy and confocal laser scanning microscopy for turbid sample imaging**

Paweena U-Thainual  
Do-Hyun Kim

# Comparison between optical-resolution photoacoustic microscopy and confocal laser scanning microscopy for turbid sample imaging

Paweena U-Thainual and Do-Hyun Kim\*

US Food and Drug Administration, 10903 New Hampshire Avenue, Silver Spring, Maryland 20993, United States

**Abstract.** Optical-resolution photoacoustic microscopy (ORPAM) in theory provides lateral resolution equivalent to the optical diffraction limit. Scattering media, such as biological turbid media, attenuates the optical signal and also alters the diffraction-limited spot size of the focused beam. The ORPAM signal is generated only from a small voxel in scattering media with dimensions equivalent to the laser spot size after passing through scattering layers and is detected by an acoustic transducer, which is not affected by optical scattering. Thus, both ORPAM and confocal laser scanning microscopy (CLSM) reject scattered light. A multimodal optical microscopy platform that includes ORPAM and CLSM was constructed, and the lateral resolution of both modes was measured using patterned thin metal film with and without a scattering barrier. The effect of scattering media on the lateral resolution was studied using different scattering coefficients and was compared to computational results based on Monte Carlo simulations. It was found that degradation of lateral resolution due to optical scattering was not significant for either ORPAM or CLSM. The depth discrimination capability of ORPAM and CLSM was measured using microfiber embedded in a light scattering phantom material. ORPAM images demonstrated higher contrast compared to CLSM images partly due to reduced acoustic signal scattering. © 2015 Society of Photo-Optical Instrumentation Engineers (SPIE) [DOI: [10.1117/1.JBO.20.12.121202](https://doi.org/10.1117/1.JBO.20.12.121202)]

Keywords: photoacoustic microscopy; confocal microscopy; lateral resolution; turbid media; Monte Carlo simulation.

Paper 150287SSRR received Apr. 30, 2015; accepted for publication Jul. 17, 2015; published online Aug. 10, 2015.

## 1 Introduction

Photoacoustic imaging combines the physics of optics and acoustics, providing the advantage of optical modality in terms of high resolution and the advantage of acoustic modality in terms of high penetration depth.<sup>1</sup> Short optical pulses usually ranging from a few nanoseconds to microseconds generate surface or subsurface acoustic ultrasound waves when the pulses are irradiated on photon-absorbing structures in biological samples. Computational image reconstruction using generated acoustic signals collected by ultrasound transducers or microphones is the basis of photoacoustic imaging, which can be categorized into two types: (1) photoacoustic tomography (PAT), which computationally reconstructs tomographic images by processing acoustic waves generated in a relatively large area using a spatially expanded pulsed laser source and (2) photoacoustic microscopy (PAM), which uses focused laser irradiation that excites a small volume, produces acoustic waves, and then is detected by a transducer. Further details on photoacoustic imaging can be found in a recent review paper.<sup>2</sup> PAM also can be categorized into two types depending on resolution: (1) acoustic-resolution PAM (ARPAM), which uses focused laser irradiation with spot sizes slightly larger than the transducer, and thus, lateral and axial resolutions are determined by transducer numerical aperture (NA) and detection time gating, respectively,<sup>3</sup> and (2) optical-resolution PAM (ORPAM), which excites the sample with an optically diffraction-limited

laser spot, and thus, both lateral and axial resolutions are determined by optical characteristics of the focused beam.<sup>4</sup>

A standard characterization method for photoacoustic imaging, especially for resolution measurement, has not been established. Various efforts have been made to measure lateral resolution.<sup>5-9</sup> For PAM, lateral resolution is traditionally measured using a patterned resolution target such as the U.S. Air Force (USAF) 1951 bar chart.<sup>10</sup> Targets comprised of a patterned thin metal film (PTMF) and photon-absorbing lines printed on transparent film were used to measure lateral resolution for PAT.<sup>11,12</sup>

Thin metal film is highly effective in generating photoacoustic signal due to the high absorption coefficient of metal. Moreover, thin films are optimal for generating sound waves perpendicular to the target surface. Propagation of sound waves in the direction perpendicular to the surface of chromium film from laser irradiation was extensively studied by Ko et al.<sup>13</sup> Sound waves with different parameters (amplitude, frequency, etc.) can be formed by different generation mechanisms; however, the strongest ultrasound signal is generated from a surface vibration in the direction perpendicular to the surface. In this study, PTMF is used to measure lateral resolution of ORPAM in comparison to confocal laser scanning microscopy (CLSM).

The major advantage of CLSM over other wide-field microscopy is its scattered-light rejection capability.<sup>14</sup> Only the signal from the objective lens focal spot is collected by the detector pinhole; consequently, CLSM has been proven to be highly

\*Address all correspondence to: Do-Hyun Kim, E-mail: [do-hyun.kim@fda.hhs.gov](mailto:do-hyun.kim@fda.hhs.gov)

useful for imaging microscopic structures through turbid biological samples. ORPAM is frequently used in a quasiconfocal arrangement, where the laser objective focal spot and ultrasound collection transducer overlap. However, since the transducer NA does not contribute to the ORPAM system resolution, and since the ORPAM acoustic signal is not scattered in its path to the transducer (in contrast to the CLSM optical signal that must pass through scattering material in its return path to the photodetector), a difference in magnitude of scattered-light rejection is expected between ORPAM and CLSM.

In this paper, we present assessment of a multimodal optical microscopy platform that provides the dual capabilities of ORPAM and CLSM. ORPAM lateral resolution was measured using PTMF with and without overlying scattering media. Also studied in this work is the scattered-light rejection capability and depth discrimination of an ORPAM system in comparison to CLSM using different NA lenses and time gating. The computational results based on Monte Carlo simulations were used to compare the effect of scattering media on the lateral resolution of ORPAM.

## 2 Experiments

### 2.1 Multimodal Microscopy System

The multimodal microscopy system operated in transmission mode and used a galvanometer pair for scanning. The schematic of the multimodal microscopy system is shown in Fig. 1. The laser source is a pulsed dye laser with Rhodamine 6G dye (Sirah, Spectra Physics, Santa Clara, California). The laser repetition rate was set at 2000 Hz, with 570-nm wavelength, pulse duration of 7 to 10 ns, and each pulse had energy of 10 to 20 nJ depending on the setting. Since there were energy fluctuations between pulses, laser output was monitored by an amplified photodiode (Photo Diode 1, PDA55, Thorlabs, Newton, New Jersey), to which each photoacoustic signal was normalized. The monitor energy pulses were also used to trigger data acquisition. The laser output was then controlled by a variable neutral density filter (NDC-100C-4, Thorlabs) before it was coupled to a single-mode fiber. One of the two output ports of the fiber coupler was used to measure and monitor laser energy delivered to the target, and the other was used for ORPAM. The ORPAM illumination output from the single-mode fiber was collimated to a 3-mm diameter beam. A 10:90 beam splitter (BSN04, Thorlabs) was placed in front of *x-y* galvo scanners to direct light toward the CLSM photodetector (Photo Diode 2, PDA55, Thorlabs). Galvo scanner mirrors (GVS202, Thorlabs) were driven by a computer-controlled data acquisition card (USB-6211, National Instruments, Austin, Texas). Achromatic doublet lenses were used to relay the conjugates to the objective. Achromatic doublets have some spherical aberrations, so the vergence angle was kept small by limiting the galvo scanner driving voltage much lower than maximum driving voltage (2.0 V). Two objective lenses were tested: one with NA = 0.28 (10× Plan Apo, Mitutoyo, Aurora, Illinois) and the other with NA = 1.0 (40× W Plan-apochromat, Zeiss, Jena, Germany). The generated photoacoustic signal was collected with a focused transducer (A326S-SU, 4.9-MHz center frequency, 15.31-mm focal length, -6 dB bandwidth 58.83%, Olympus NDT Panametrics, Tokyo, Japan) for transmission mode and a nonfocused transducer (I1-0204S-SM, 2.31 MHz center frequency, -6 dB bandwidth 49.37%, Olympus NDT Panametrics, Tokyo, Japan) for epi-illumination mode operation. The ORPAM signal was amplified with a

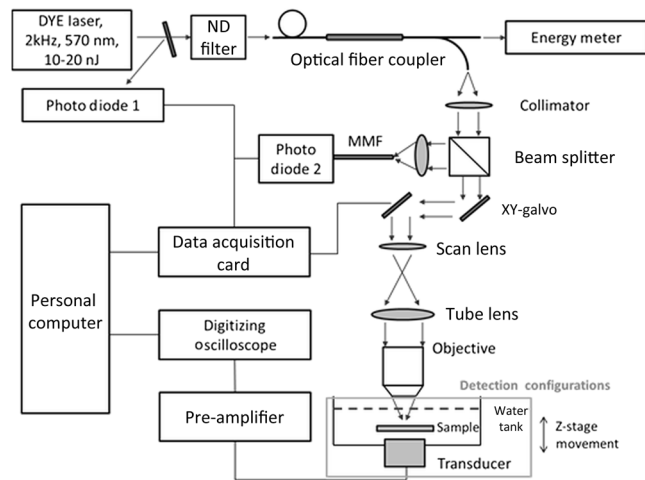


**Fig. 1** Schematic of multimodal optical-resolution photoacoustic microscopy (ORPAM) and confocal laser scanning microscopy (CLSM) system. ND stands for neutral density and MMF stands for multimode fiber.

54-dB preamplifier (5662, Olympus, Tokyo, Japan) and then digitized using a digital oscilloscope (USB-5133, 100 MS/s, National Instruments). The back-reflected signal was detected on photodiode 2 for confocal microscopy. A multimode optical fiber with NA = 0.22 and core diameter of 105  $\mu\text{m}$  (M15L01, Thorlabs) was used as the confocal pinhole. Light was focused on the fiber with a NA = 0.25 focusing lens (F810SMA-635, Thorlabs).

The detection configurations for the samples in the ORPAM system are shown in Fig. 2.

- (1) The forward-1 configuration is a transmission mode, where the laser and transducer are set on opposite sides of the sample (top and bottom, respectively). The laser is transmitted through the sample and generates a photoacoustic signal that is collected with a transducer at the bottom. In the forward-1 configuration, the sample pattern faces downward toward the transducer and is submerged in water. As a result, the laser is transmitted through the turbid media inside the cuvette, glass, and sample pattern. This configuration is used for lateral resolution measurement.
- (2) The forward-2 configuration is similar to forward-1, but the sample pattern is embedded in the turbid media. Also, the generated sound waves propagate in turbid media instead of water. This setup allows us to observe the effect of scattering media in various depths, unlike the forward-1 configuration in which the turbid media depth is limited to the cuvette thickness. Therefore, this configuration is used for depth discrimination measurement.
- (3) The backward-3 configuration is a reflection mode where the laser and transducer are both set above the sample, as shown in Fig. 2(c). The sample pattern with an overlying layer of turbid media faces up toward the laser and transducer. The laser is transmitted through the turbid media and sample pattern, which are both immersed in water. The backward

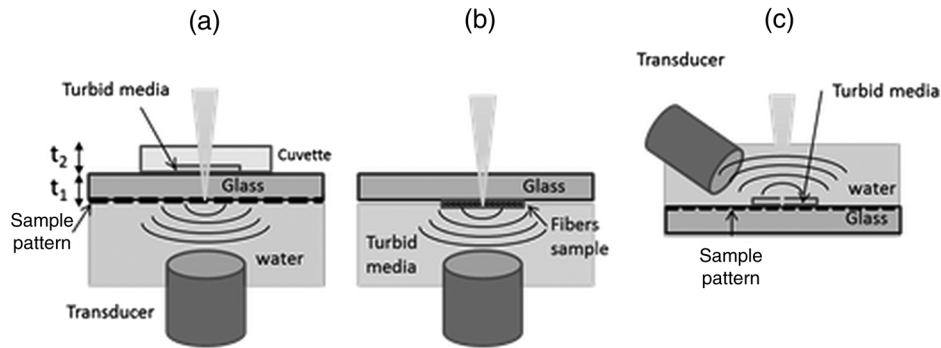


**Fig. 2** Various sample configurations used in this study; (a) Forward-1; (b) Forward-2; (c) Backward-3.  $t_1$  is the thickness of glass (1 mm) and  $t_2$  is the thickness of the cuvette (1 mm), which provides 100  $\mu\text{m}$  space for containing scattering material.

propagating photoacoustic signal is collected by the transducer on the top beside the laser. It is used for lateral resolution measurement.

In the forward-1 configuration, the optical beam makes a single pass through the turbid media. In the forward-2 configuration, the optical beam does not pass through the turbid media. In the backward-3 configuration, the optical beam makes a double pass through the turbid media.

In this study, we normalized ORPAM and CLSM signals from each pulse, because there are fluctuations in the energy level of each pulse. Therefore, the ORPAM and CLSM were not operated simultaneously because one of the digitizer input channels was used for obtaining single-pulse energy from each pulse for normalization.

## 2.2 Samples

A commercially available USAF 1951 resolution bar-chart pattern (NT57-895, Edmund Optics, Barrington, New Jersey), which is comprised of chromium film deposited on a 2-mm fused silica glass [Fig. 3(a)], was used for measuring the diffraction-limited lateral resolution of the ORPAM system. Thin chromium film generates strong photoacoustic signals<sup>11</sup> and is robust enough for focused illumination. However, applied laser radiant exposure ( $\text{J}/\text{cm}^2$ ) must be carefully adjusted when imaging through turbid media because the damage threshold of thin chromium film is lower than that of biological samples. For this reason, a custom PTMF with scattering barrier was developed for comparison of ORPAM and CLSM lateral resolution. The

custom PTMF target was prepared by laser-etching thin chromium film coated on the 2-mm glass substrate. The output of the pulsed dye laser was increased to a level higher than the chromium thin film damage threshold. The output energy per pulse was 10 to 20 nJ for imaging and increased from 40 to 60 nJ for etching. A high  $\text{NA} = 0.85$  dry lens was used to achieve finer etching lines. Multiple X-shapes were etched on the custom PTMF for testing lateral resolution [Fig. 3(b)].

The microscopic image of a fiber sample we prepared for depth discrimination testing is shown in Fig. 3(c). Black and red fibers of cotton and wool were attached to the 1-mm-thick glass surface using adhesive film surrounding the central area, so that fibers in the central area can float in liquid providing different depths. The fibers had thickness ranging from 10 to 50  $\mu\text{m}$ .

For lateral resolution measurement, the turbid scattering barrier was prepared using a 100- $\mu\text{m}$  cuvette, which contained 0%, 4%, 7%, and 10% Intralipid® with corresponding scattering coefficient ( $\mu_s$ ) of <0.003/cm, 210/cm, 325/cm, 443.6/cm, respectively. The optical properties of Intralipid were calculated using a method described elsewhere.<sup>15</sup> To measure the effect of scattering on depth discrimination, scattering material was prepared using 1% intralipid with  $\mu_s = 90.26/\text{cm}$ .

## 3 Numerical Calculations

### 3.1 Image Formation in Turbid Media

Light scattering attenuates signal strength and affects resolution and contrast when imaging a turbid object. Conventional optical

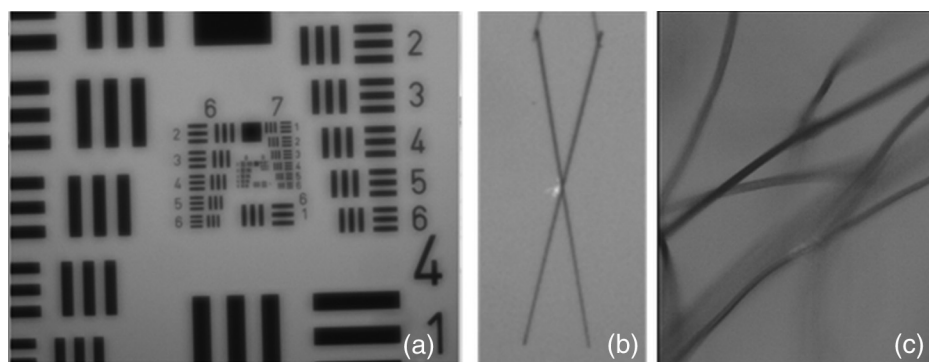


**Fig. 3** Charge-coupled device (CCD) images of (a) resolution target USAF 1951 (b) X-pattern etched on thin chromium film coated glass; (c) red and black microfibers sample (10 to 50  $\mu\text{m}$ , wool/cotton).

imaging systems use various techniques to overcome scattering. For example, multiphoton microscopy is spatially confined within the interaction volume of the high-intensity light field by the nonlinear fluorescent excitation process. Optical coherence tomography likewise achieves depth sectioning by using a different mechanism of coherence gating, which is inherently a single-scattering phenomena. CLSM uses a pinhole at a conjugate focal plane to reject out-of-plane light scattered from adjacent voxels in the sample. The smaller the pinhole, the greater the ability of CLSM imagers to reject scattered light and collect ballistic photons. However, a smaller pinhole restricts the total number of photons collected, resulting in poor signal-to-noise ratio (SNR). Reduced contrast and SNR are mainly due to the reduced signal strength from the focal volume.<sup>16,17</sup> Reduced resolution is mostly due to enlarged focal volume by scattered photons. Since the CLSM signal is predominantly comprised of the contribution from ballistic (i.e., single scattered) photons from the focal volume, the effect of scattering on reduced resolution is a consequence of reduced ballistic photons passing through the pinhole. Thus, the resolution and depth-discrimination capabilities of CLSM are less affected by the scattering process itself but are rather governed by the system confocality.

On the other hand, ORPAM image formation in turbid media is slightly different from CLSM. The biggest difference is the lack of a pinhole for ORPAM. However, ORPAM can be operated in quasicongocal mode when the focal volume of the transducer overlaps that of the objective lens. However, the acoustic focal volume of a highly focused transducer is still larger than the optical focal volume of the objective lens.<sup>18</sup> Therefore, the scattered-light rejection capability of ORPAM is much lower than CLSM. Thus, time-gating is necessary for ORPAM to achieve image sectioning through turbid media. Depending on the central frequency and bandwidth of the transducer and on the temporal resolution of the preamplifier and digitizer, ORPAM can achieve very high sectioning capability. For illustration, the speed of sound in water is  $\sim 1500$  m/s, which requires a temporal resolution of 1 ns to achieve  $1.5\text{-}\mu\text{m}$  axial resolution. Similar to the compromise between resolution and SNR described above for CLSM, high-resolution time-gating sacrifices transducer signal strength.

Another difference between ORPAM and CLSM is the lateral resolution. CLSM rejects unwanted scattered light from the optical focal volume of the objective lens, thus achieving diffraction-limited resolution in both axial and lateral directions. ORPAM achieves high-axial resolution by time-gating, but its lateral resolution is strictly governed by the spatial energy

distribution profile of the illuminating laser focal volume. If optical energy delivered to the sample is strong enough to generate a detectable photoacoustic signal, then the signal will be transmitted to the transducer and recorded as a feature in the ORPAM image regardless of the nature of the scattered photon (ballistic or multiscattered). Hence, the ORPAM acoustic signal, in contrast to the CLSM optical signal, does not include a double-pass through scattering media. Theoretically, ORPAM has an advantage in signal strength due to this fact. However, in reality, the photoacoustic signal for ORPAM and the optical signal for CLSM (either reflection or fluorescence) cannot be compared directly, making quantitation of this advantage difficult.

The lateral resolution of an optical imaging system will be reduced by both scattering and a reduction in SNR. The calculations of Liu et al.<sup>18</sup> show that the focal spot size in the lateral direction is 14% larger when the photon passes 1.1-times the scattering mean free path, while a more significant increase is calculated for 1.7-times mean free path.

### 3.2 Monte Carlo Simulation

A Monte Carlo simulation<sup>15</sup> was used in this study to estimate degradation in the lateral resolution of ORPAM when imaging through turbid media. Monte Carlo simulations have been used by many research groups with great success to simulate photon scattering in turbid media. Each photon propagates in turbid tissue independently, so only fundamental rules for absorption, scattering, reflection, and refraction are needed to simulate a large number of photons (millions). We implemented our Monte Carlo simulation on a quad-core CPU personal computer using 1.5 million photons. Computation time for each simulation was 10 min.

### 3.3 Monte Carlo Simulation Results

The Monte Carlo simulation of light scatter through a turbid medium in this study produces two outputs. First, the fluence distribution of the focal spot with and without the turbid medium [Figs. 4(b) and 5(b)] is calculated to predict the degradation of lateral resolution due to scattering. The scattering-layer thickness was  $100\ \mu\text{m}$  and 10% intralipid with  $\mu_s = 443/\text{cm}$  was used. The anisotropy and absorption coefficients were 0.84 and  $0.004/\text{cm}$ , respectively.<sup>19</sup> The second simulation output describes the effect of the location of the scattering layer. Figure 6(a) shows the geometry of the scattering layer 1.0 mm above the target region. This geometry is used to simulate the sample shown in Fig. 2(a). Convergence of the simulation was ensured by increasing the number of launched photons until the

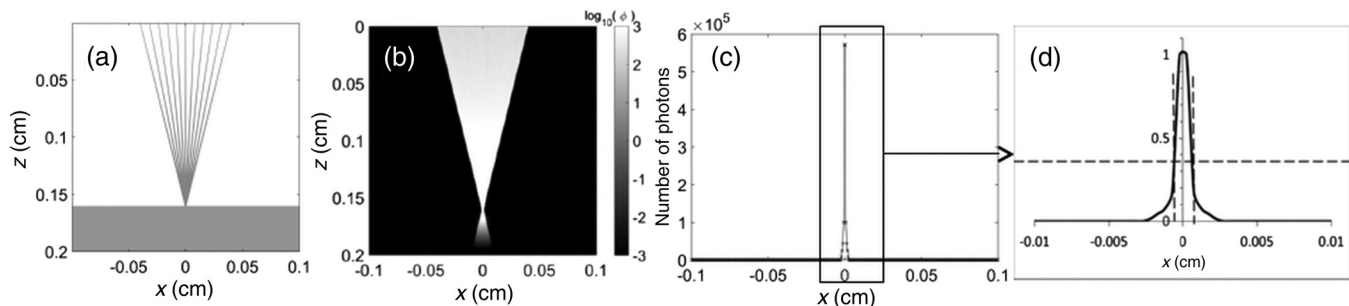


**Fig. 4** (a) Layout of the sample layer and optical path (cone lines); (b) fluence distribution shows no scattering but only absorption at the sample layer; (c) the lateral beam profile at the surface of the sample layer; and (d) zoom-in of normalized beam profile shows the nominal beam radius at  $1/e$  (dotted line) of  $12\ \mu\text{m}$ .

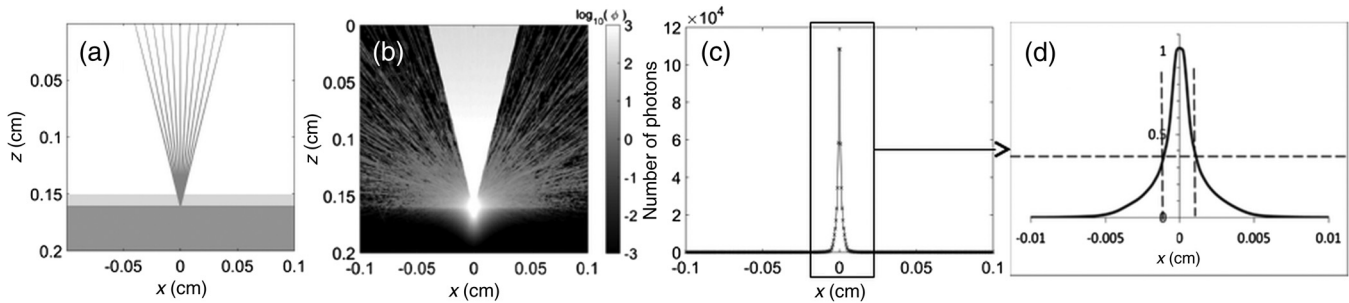


**Fig. 5** (a) Layout of the sample layer (thick layer), the scattering barrier (thin layer), and optical path (cone lines); (b) fluence distribution clearly shows light scatter; (c) the lateral beam profile at the surface of the sample layer; (d) zoom-in of normalized beam profile shows the nominal beam radius at 1/e (dotted line) was increased to 25  $\mu\text{m}$ .

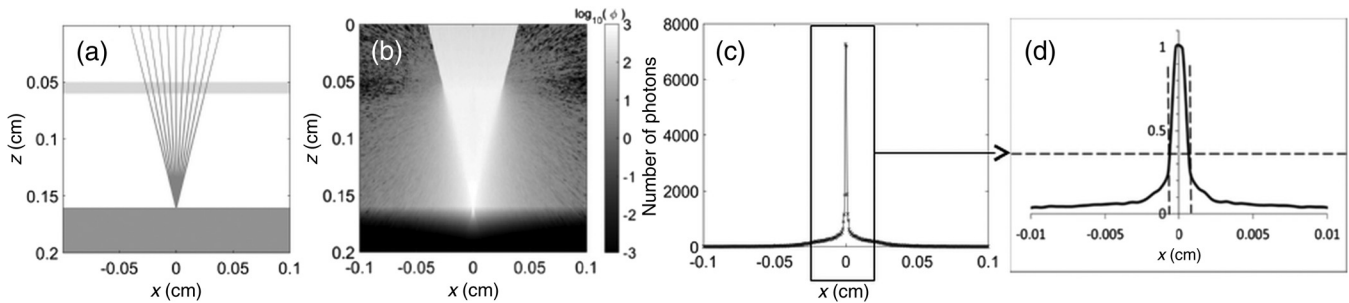


**Fig. 6** (a) Layout of the sample layer (thick layer at the bottom), white layer represents glass, the scattering barrier (thin layer), and optical path (cone lines); (b) fluence distribution shows scattered photons distributed in wider spatial range; (c) the lateral beam profile at the surface of the sample layer; and (d) zoom-in of normalized beam profile shows the nominal beam radius at 1/e (dotted line) was decreased to 14  $\mu\text{m}$ .

resulting data are consistent. All simulations used 4.5 million photons. The 1/e radius of the laser beam at the top of the tissue layer for Figs. 4(c), 5(c), and 6(c) was 12, 25, and 14  $\mu\text{m}$ . This simulation result indicates that line broadening due to the scattering layer in the forward-1 geometry is negligible, because scattered light from the barrier 1 mm away from the tissue surface increases the background noise level uniformly over a large area. However, as can be seen from Fig. 5(c), the forward-2 geometry doubles the focused spot size due to the scattering layer being in contact with the tissue layer. A comparison of simulation and experimental results will be discussed in the following section.

**Table 1** Nominal width of a single line of Group 8 in each element and number of line pairs/mm of USAF 1951.

Element	Width of a single line		Number of line pairs / mm	
	Group 8 ( $\mu\text{m}$ )	Group 8 (lp/mm)	Group 8 (lp/mm)	Group 8 (lp/mm)
1	1.95	256.0		
2	1.74	287.0		
3	1.55	323.0		
4	1.38	362.0		
5	1.23	406.0		
6	1.1	456.0		

## 4 Results and Discussion

### 4.1 Lateral Resolution of ORPAM Without Scattering

The lateral resolution of ORPAM and CLSM was measured using a USAF 1951 patterned thin film test target without scattering barrier. The width of a single line of Group 8 in each element of USAF 1951 is shown in Table 1. As shown in Fig. 7, the three lines of element 8-5 were distinguished in the ORPAM image when using Rayleigh's criteria.<sup>20</sup> CLSM generated similar lateral resolution (not shown). The pattern spacing of element 8-5 is 1.23  $\mu\text{m}$ , which corresponds well

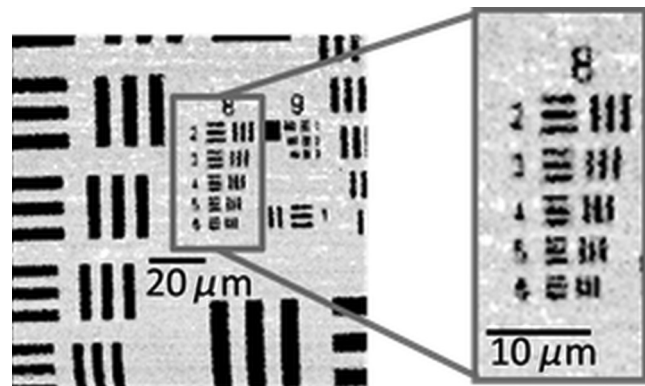


**Fig. 7** ORPAM image of USAF 1951 resolution target around group 8.

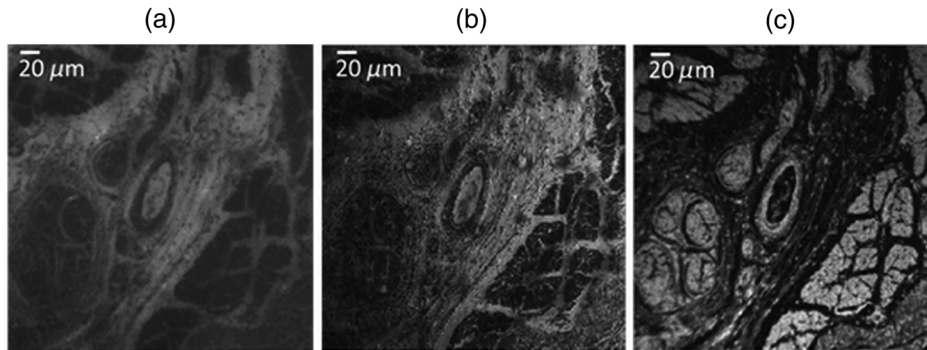


**Fig. 8** Images of fixed human skin section through sweat gland image from (a) CCD, (b) CLSM, and (c) ORPAM.

to the theoretical diffraction-limited spot size of 1.24 calculated using  $NA = 0.28$  lens and wavelength ( $\lambda$ ) 570 nm:

$$W_0 = \frac{0.61 \times \lambda}{NA} \quad (1)$$

Thus, the ORPAM and CLSM achieved diffraction-limited performance absent scattering media.

Thin chromium film of USAF 1951 provides both high reflectivity and absorption, which is obviously not a feature of a biological sample. A pre-prepared biological fixed slide of human skin section through sweat gland was tested for ORPAM and CLSM imaging, as shown in Fig. 8. The slide was stained with eosin and methylene blue.

#### 4.2 Lateral Resolution Comparison in Turbid Media

According to the analysis and Monte Carlo simulations described in the previous section, a 100- $\mu\text{m}$ -thick scattering barrier with  $\mu_s = 443.6/\text{cm}$  for the configurations shown in Figs. 2(a) and 2(c) will produce  $\sim 1.2$  times and 2 times larger laser spot size in comparison to the configurations without scattering. Figure 9

shows images of Groups 8 of USAF 1951 resolution target using ORPAM and CLSM with and without scattering barrier for forward-1 and backward configurations. Although 1.2-times and 2-times increase in the focal spot size is expected for forward-1 and backward configurations, corresponding CLSM images in Fig. 9 resolved the similar element 8-5 pattern of the resolution target. Our system uses an optical fiber with  $NA = 0.22$  and a focusing lens with  $NA = 0.25$ . This combination maintains a significant degree of confocality between lens-dominated and fiber-dominated configurations,<sup>21</sup> providing signal collection efficiency when high-sensitivity detectors such as photomultiplier tubes are not used. The lateral resolution degradation was minimal for CLSM with the given scattering parameters in our setup.

The ORPAM images in Fig. 9 show greater degradation in lateral resolution in the backward configuration compared to the forward-1 configuration.

The degraded lateral resolution with scattering was further studied using the X-shaped PTMF fabricated by laser etching. The scattering barrier was prepared using a 100  $\mu\text{m}$ -thick cuvette that contained 0%, 4%, 7%, and 10% intralipid solution.

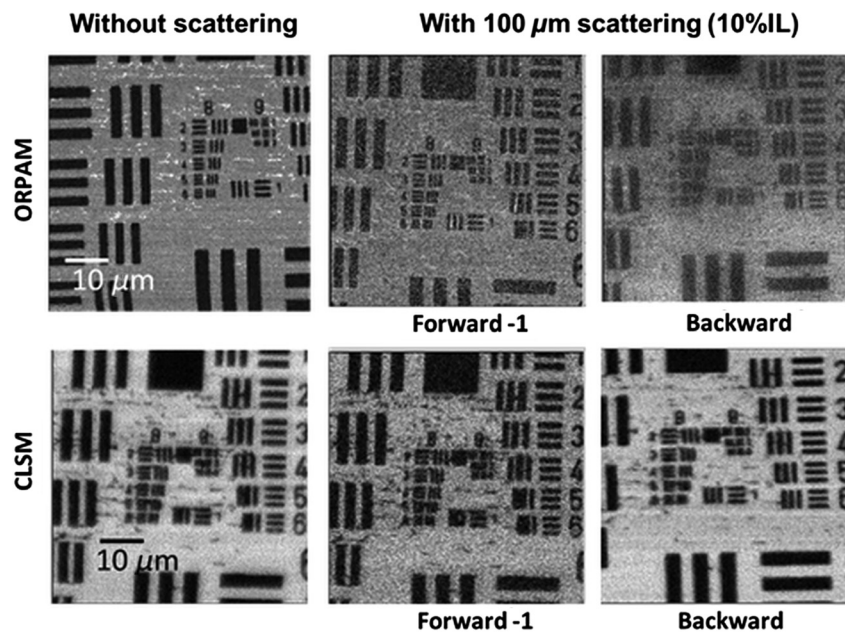


**Fig. 9** Images of USAF 1951 resolution test target using ORPAM and CLSM with and without scattering media. Backward configuration images were flipped for easy comparison.

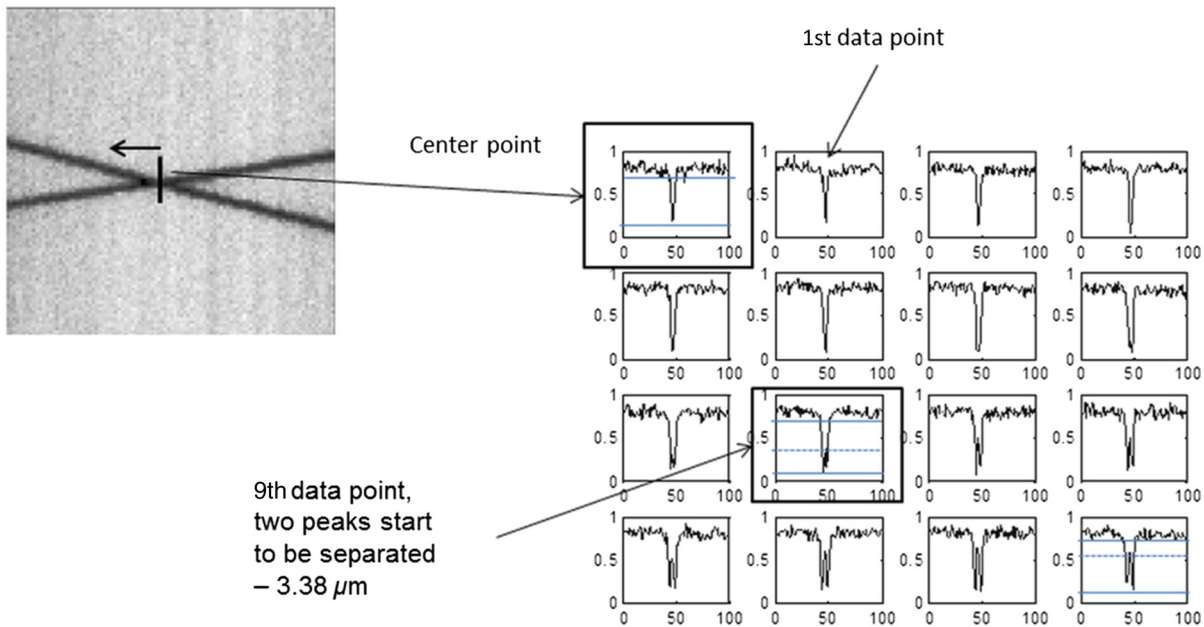


**Fig. 10** CLSM image of X-patterned thin metal film (PTMF) with 0% intralipid barrier; corresponding intensity profile of two separated etched lines along the direction shown as black arrow. The two-peak signals represent two separated etched lines, as shown in the ROI box.

An intensity profile was measured along the black arrow, as shown in Fig. 10. We used Rayleigh's criteria to distinguish two intensity dips of the separated etched lines by quantifying the depth of the middle dip with respect to the peak, as shown in Fig. 11. CLSM showed little degradation in lateral resolution as the concentration of intralipid scattering barrier increased. ORPAM showed slightly higher dependence of scattering in terms of lateral resolution degradation. The result agrees with our previous observation.

### 4.3 Effect of Scattering on Depth Discrimination, $NA = 1.0$ Objective

We used fibers and scattering material for depth discrimination comparison between ORPAM and CLSM.

CLSM and ORPAM images of wool and cotton fibers submerged in water and 1% intralipid solution are shown in Fig. 12. The objective lens NA was 1.0. When the fibers were submerged in water alone, the CLSM images showed higher contrast and

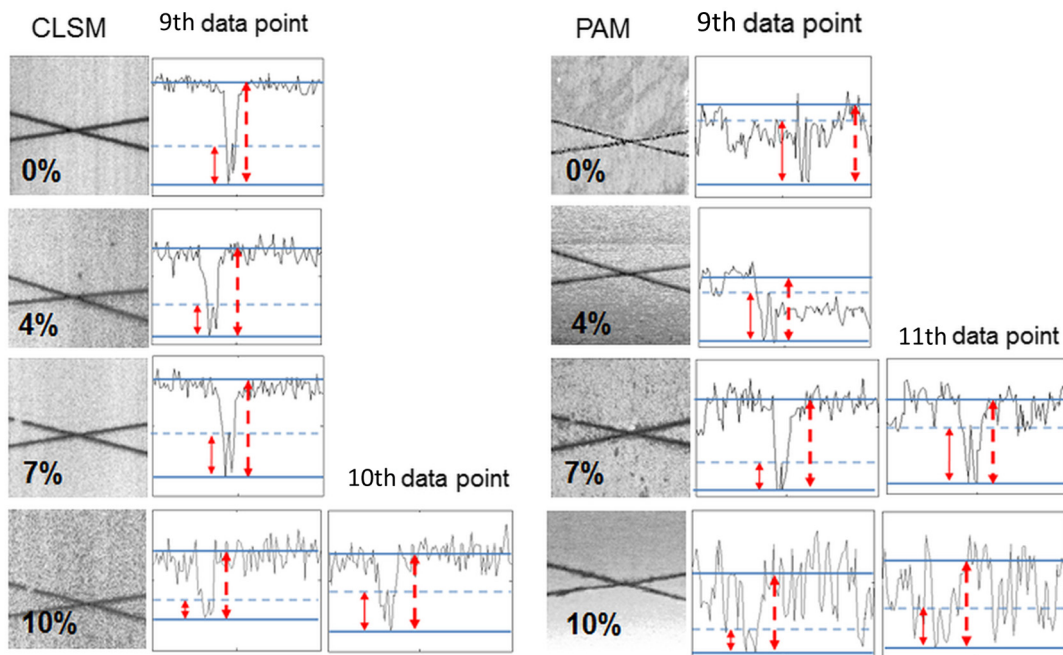


**Fig. 11** CLSM and ORPAM images of X-patterned PTMF with 0%, 4%, 7%, and 10% intralipid barrier; the two-peak signals represent two separated etched lines. Rayleigh's criterion was used by quantifying the depth of the middle dip (solid line) with respect to the peak (dashed line).

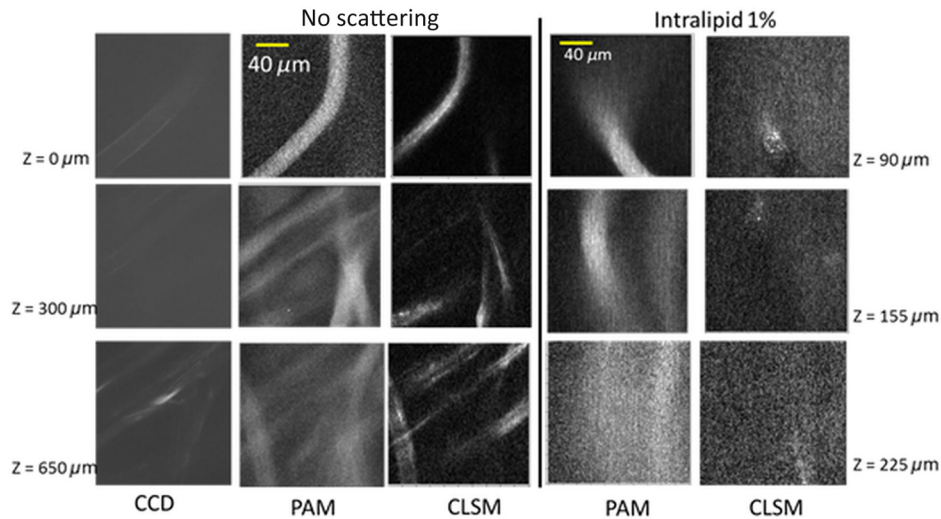


**Fig. 12** CLSM and ORPAM images of wool and cotton fibers submerged in water and 1% intralipid solution, using  $NA = 1.0$  objective lens.

better depth discrimination in comparison to maximum amplitude projection (MAP) ORPAM images. Our current digitizer had a low sampling rate (100 MS/s), thus only 100 data points were used for ORPAM signal, which were enough to contain all the signals from a single laser pulse. MAP was established using these 100 data points from each laser pulse. The relatively high contrast of CLSM images is also partly due to the higher signal collection efficiency of the objective lens with  $NA = 1.0$ . As expected, the CLSM and ORPAM image quality had minimal dependence on depth.

When 1% intralipid solution was used, the CLSM images were severely affected by signal loss due to scatter. The signal level collected at  $Z = 90 \mu\text{m}$  depth was significantly lower than at the top surface. This is a reasonable result considering the fact that 1% intralipid solution has 10 times higher scattering than human skin. A confocal microscope with 1064-nm illumination is reported to have an imaging depth up to  $350 \mu\text{m}$ ,<sup>22</sup> thus considering the higher  $\mu_s$  of 1% intralipid and shorter wavelength (570 nm), and the penetration depth is expected to be lower. On the other hand, ORPAM visualized target fibers at greater depths. The reason for rapid degradation of signal strength for the CLSM images is likely the double optical path, i.e., the photons must go through the scattering layer twice for illumination and signal detection. However, ORPAM is affected by the optical scattering only for illumination; thus, ORPAM provides higher signal strength in the presence of scattering.

#### 4.4 Effect of Scattering on Depth Discrimination, $NA = 0.28$ Objective

Figure 13 shows CLSM and ORPAM images of wool/cotton fibers submerged in 1% intralipid solution using  $NA = 0.28$  objective lens. The signal collection efficiency of CLSM is theoretically lower for a lower NA objective. However, the signal level recorded by the photodetector was about 10 times higher for  $NA = 0.28$  lens compared to  $NA = 1.0$  lens. Also, the CLSM images of fibers in 1% intralipid solution were slightly brighter than for  $NA = 1.0$  lens, as shown in Fig. 12. This is believed to be the lower effect to the resolution by scattering when the NA of the objective lens is lower. The ORPAM images for  $NA = 0.28$  lens were very similar to the previous results with  $NA = 1.0$  lens.

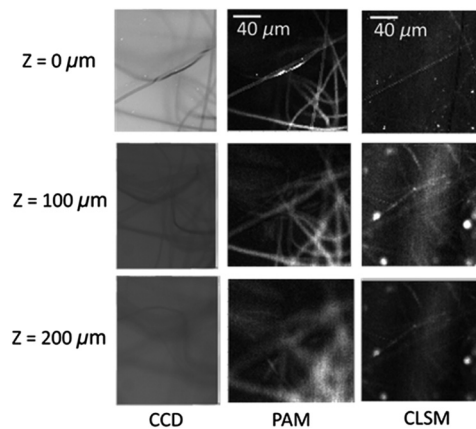


**Fig. 13** CLSM and ORPAM images of wool/cotton fibers submerged in 1% intralipid solution, using  $NA = 0.28$  objective lens.

#### 4.5 Time-Gating Depth Discrimination Capability of ORPAM

We used a time-gating scheme to improve the depth discriminating capability of ORPAM. Unlike CLSM, ORPAM does

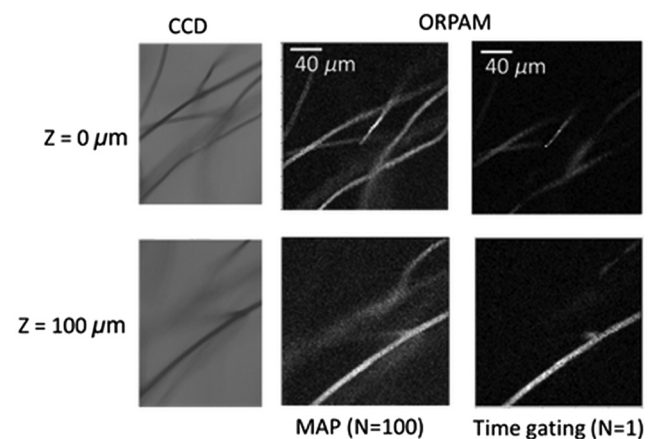


**Fig. 14** CCD and ORPAM en face images of fiber embedded in 1% intralipid solution with or without time gating.

not have inherent depth discrimination capability, so it needs time-gating to choose the image focal plane. The second column of Fig. 14 is ORPAM MAP images using  $N = 100$  data points, while the third column shows time-gating of the ORPAM with  $N = 1$  data point, where  $N$  is the total number of data used to reconstruct the MAP image both in depth and time. Time-gating of our system is limited by the digitizer, which has a 100 MS/s sampling rate. This sampling rate equals a temporal resolution of 0.01  $\mu$ s, which is equivalent to a  $\sim 15$ - $\mu$ m depth section in water. For better depth discrimination using time-gating, a higher speed digitizer is necessary. Also, sectioning by time-gating is fundamentally different from sectioning by a quasiconfocal effect, so no improvement in the lateral resolution is expected from time-gating.

## 5 Conclusion

A multimodal optical microscopy platform that provides capability of ORPAM and CLSM was constructed, and the lateral resolution of both modes was measured using PTMF with and without a scattering barrier. The effect of scattering media on the lateral resolution was studied using different scattering coefficients and was compared to computational Monte Carlo simulations.

The lateral resolution measurements for CLSM showed less dependence on scattering, whereas the lateral resolution measurements for ORPAM showed slightly higher dependence. The axial resolution cannot be obtained in this study because the test target USAF 1951 can provide micrometer resolution in lateral direction but not in axial direction. However, as far as we understand, no samples are available for micrometric precision axial resolution imaging. Our sample using fibers was the best we could do at this time. Our future plans include developing such a high precision axial resolution target.

We found no significant degradation of lateral resolution due to optical scattering for either ORPAM or CLSM when using the  $NA = 0.28$  objective lens. This confirms that the effect of scatterer is lower when the  $NA$  is lower. The depth discrimination capability of ORPAM and CLSM was studied using microfiber embedded in light-scattering phantom material. The ORPAM images demonstrated higher contrast compared to CLSM images, partly due to lower scattering in the optical-acoustic signal path compared to the optical-optical signal path for the CLSM arrangement. The results of the time-gating shows clear improvement in the axial resolution of ORPAM. However, we did not compare this study to CLSM because the current digitizer is limited in sample speed by 100 MS/s. This gives  $\sim 15$ - $\mu$ m axial resolution in time-gating, which is about 15 times poorer than that of confocal microscope. Therefore, we did not directly compare the depth discrimination capabilities of both modalities. Our future plan is to use a higher speed digitizer along with a new axial resolution phantom, which will give us the opportunity to directly compare ORPAM and CLSM axial resolution.

## Acknowledgments

This work was supported in part by the Medical Countermeasures Initiative of the U.S. Food and Drug Administration. The mention of commercial products, their sources, or their use in connection with material reported herein is not to be construed as either an actual or implied endorsement of such products by the Department of Health and Human Services.

## References

1. M. Xu and L. V. Wang, "Photoacoustic imaging in biomedicine," *Rev. Sci. Instrum.* **77**, 041101 (2006).
2. P. Beard, "Biomedical photoacoustic imaging," *Interface Focus* **1**, 602–631 (2011).
3. S. Park et al., "Acoustic resolution photoacoustic microscopy," *Biomed. Eng. Lett.* **4**, 213–222 (2014).
4. Y. Yuan, S. Yang, and D. Xing, "Optical-resolution photoacoustic microscopy based on two-dimensional scanning galvanometer," *Appl. Phys. Lett.* **100**, 023702 (2012).
5. W. Shi et al., "Optical resolution photoacoustic microscopy using novel high-repetition-rate passively Q-switched microchip and fiber lasers," *J. Biomed. Opt.* **15**(5), 056017 (2010).
6. R. L. Shelton and B. E. Applegate, "Ultra-high resolution photoacoustic microscopy via transient absorption," *Biomed. Opt. Exp.* **1**(2), 676–686 (2010).
7. W. Shi et al., "In vivo dynamic process imaging using real-time optical-resolution photoacoustic microscopy," *J. Biomed. Opt.* **18**(2), 026001 (2013).
8. Z. Xie et al., "Laser-scanning optical-resolution photoacoustic microscopy," *Opt. Lett.* **34**(12), 1771–1773 (2009).
9. C. Zhang et al., "Label-free photoacoustic microscopy of cytochromes," *J. Biomed. Opt. Lett.* **18**(2) 020504 (2013).
10. K. Maslov et al., "Optical-resolution photoacoustic microscopy for in vivo imaging of single capillaries," *Opt. Lett.* **33**, 929–931 (2008).
11. D. H. Kim et al., "Patterned thin metal film for the lateral resolution measurement of photoacoustic tomography," *Biomed. Eng. Online* **11**, 37 (2012).
12. X. Wang et al., "Photoacoustic tomography of biological tissues with high cross-section resolution: reconstruction and experiment," *Med. Phys.* **29**, 2799–2805 (2002).
13. S. H. Ko et al., "Laser induced short plane acoustic wave focusing in water," *Appl. Phys. Lett.* **91**, 051128 (2007).
14. M. Petran et al., "Tandem scanning reflected-light microscope," *J. Opt. Soc. Am. A* **58**, 661–664 (1968).
15. S. L. Jacques, T. Li, and S. A. Prahl, "mcxyz.c," Oregon Medical Laser Center, <http://omlc.org/software/mc/mcxyz/index.html> (1 December 2014).
16. J. M. Schmitt, A. Knüttel, and M. Yadlowsky, "Confocal microscopy in turbid media," *J. Opt. Soc. Am. A* **11**, 2226, (1994).
17. X. S. Gan, S. P. Schilders, and M. Gu, "Image formation in turbid media under a microscope," *J. Opt. Soc. Am. A* **15**, 2052 (1998).
18. Y. Liu, C. Zhang, and L. V. Wang, "Effects of light scattering on optical-resolution photoacoustic microscopy," *J. Biomed. Opt.* **17**, 126014 (2012).
19. S. T. Flock et al., "Optical properties of intralipid: a phantom medium for light propagation studies," *Lasers Surg. Med.* **12**, 510–519 (1992).
20. S. Ram, E. S. Ward, and R. J. Ober, "Beyond Rayleigh's criterion: a resolution measure with application to single-molecule microscopy," *Proc. Natl. Acad. Sci. U. S. A.* **103**(12) 4457–4462 (2006).
21. T. Dabbs and M. Glass, "Fiber-optic confocal microscope: FOCON," *Appl. Opt.* **31**(16), 3030 (1992).
22. M. Rajadhyaksha et al., "In vivo confocal scanning laser microscopy of human skin II: advances in instrumentation and comparison with histology," *J. Invest. Dermatol.* **113**(3) 293–303 (1999).

**Paweena U-Thainual** received her bachelor's degree in mechanical engineering from Mahidol University in 2005. She received her master's degree in biomedical engineering from Mahidol University in 2007. From 2008, she worked in the Percutaneous Surgery Laboratory (Perk Lab) at Queen's University, pursuing the PhD degree. She received her PhD in medical robotics from Queen's University, Canada, in 2013. Since 2014, she has been working in the Center for Devices and Radiological Health of the US Food and Drug Administration.

**Do-Hyun Kim** finished his PhD in solid state physics in 2000 at Seoul National University in the Republic of Korea. He finished his second PhD in electrical engineering with biomedical optics as the topic of his research at Johns Hopkins University in 2006. He has been performing research on biomedical optics with special interest in optical radiation safety and optical microscopy at the US Food and Drug Administration since 2006. He is a senior member of SPIE.